Research Square

Preprints are preliminary reports that have not undergone peer review.
They should not be considered conclusive, used to inform clinical practice,
or referenced by the media as validated information.

Dual Scheme Adaptive Slope-Based Filtering of Photogrammetric Point Clouds for Digital Terrain Model Generation

Muhammad Ulin Nuha

muhammad.nuha@gt.itera.ac.id

Sumatera Institute of Technology

Musa Damar Hadi

Sumatera Institute of Technology

Rizqi Aulia

Sumatera Institute of Technology

Research Article

Keywords: Slope-based filtering, Digital terrain model, UAV photogrammetry, Point cloud filtering, Surface roughness, Edge density

Posted Date: August 6th, 2026

DOI: https://doi.org/10.21203/rs.3.rs-10540222/v1

License: This work is licensed under a Creative Commons Attribution 4.0 International License.
Read Full License

Additional Declarations: No competing interests reported.

Dual Scheme Adaptive Slope-Based Filtering of Photogrammetric Point Clouds for Digital Terrain Model Generation

Muhammad Ulin Nuha (https://orcid.org/0000-0003-2731-7211)[1], Musa Damar Hadi (https://orcid.org/0009-0000-1938-9552)[1], Rizqi Aulia (https://orcid.org/0009-0007-6509-166X)[1]

[1] Study Program of Geomatics Engineering, Faculty of Infrastructure and Regional Technology, Institut Teknologi Sumatera, 35365, Lampung, Indonesia

Corresponding author: muhammad.nuha@gt.itera.ac.id

Abstract

Digital terrain models (DTMs) from unmanned aerial vehicle (UAV) photogrammetry are limited by the effectiveness of ground filtering. Conventional slope-based filtering (SBF) that utilizes a single global slope threshold is insufficient in areas with dense vegetation and closely spaced buildings. This study introduces a dual-scheme adaptive SBF that segments a photogrammetric digital surface model (DSM) into two distinct domains prior to thresholding. Scheme A, designed for variable terrain and vegetation, employs a roughness raster based on the local standard deviation of elevation. Scheme B, intended for flat, building-dominated terrain, utilizes an edge-density raster generated via Canny edge detection. Voids are addressed using a hybrid approach that combines inverse-distance-weighted and nearest-neighbor interpolation with Gaussian smoothing. The method was evaluated using an oblique UAV survey (4.15 cm ground sampling distance, 145 points per m2) covering 121 hectares of the ITERA campus in Lampung, Indonesia, an area characterized by dense secondary vegetation, buildings, and 70 meters of relief. Comparison with twelve GNSS-surveyed independent check points yielded a vertical root mean square error (RMSE) of 0.148 m and a linear error at 90% confidence (LE90) of 0.244 m. The observed 0.004 m increase over the DSM remains below the validation noise, indicating no measurable loss of terrain fidelity. However, visual inspection revealed over-smoothed surfaces in extensive vegetated regions, suggesting that void extent, rather than classification error, constitutes the primary limitation.

Keywords: Slope-based filtering; Digital terrain model; UAV photogrammetry; Point cloud filtering; Surface roughness; Edge density

1. Introduction

Basic geospatial information underpins spatial planning, infrastructure design, hazard mitigation, and natural-resource management, with the digital terrain model (DTM) serving as a core product (Ulfiah et al., 2024). A DTM represents the bare-earth surface after the removal of all above-ground objects, whereas the digital surface model (DSM) retains vegetation canopies, buildings, and other features (Z. Li et al., 2005). Downstream analyses, including hydrological routing, earthwork estimation, and contour generation for large-scale base maps, depend on bare-earth elevations. Therefore, DTM quality is primarily determined by the accuracy of terrain and non-terrain separation (Qin, Tan, Guan, et al., 2023). Unmanned aerial vehicle (UAV) photogrammetry has become the primary low-cost source of high-resolution three-dimensional data for terrain modeling (Westoby et al., 2012). Structure-from-Motion (SfM) and Multi-View Stereo (MVS) methods routinely generate dense point clouds exceeding 100 points per square meter at a fraction of the cost of airborne laser scanning. Flight and processing parameters are now sufficiently characterized to enable prediction of terrain-model accuracy based on acquisition design (Pessacg et al., 2022). Unlike airborne LiDAR, image matching reconstructs only surfaces visible in two or more images. In areas with closed canopy, photogrammetric point clouds contain few or no genuine ground returns, which prevents the filtering step from recovering terrain that was not observed (Kang et al., 2026). This asymmetry indicates that filtering algorithms adapted from LiDAR applications may not perform equivalently on photogrammetric data (Klápště et al., 2020; Yu et al., 2022).

Ground filtering algorithms are categorized into several main families, as reviewed by Qin et al. (2023): morphological filters (K. Zhang et al., 2003; Pingel et al., 2013), TIN densification (N. Chen et al., 2023; H. Li et al., 2021; Zheng et al., 2024), surface-based iterative interpolation (Kraus & Pfeifer, 1998), cloth simulation (W. Zhang et al., 2016; Cai et al., 2023), multiscale geometric approaches (C. Chen, Chang, et al., 2021; Cao et al., 2024), and slope-based filtering (Sithole & Vosselman, 2004). Slope-based filtering (SBF) classifies a point as non-terrain when the slope between it and its neighbors exceeds a specified threshold, based on the assumption that natural terrain exhibits more gradual elevation changes than the boundaries of buildings and vegetation. The main advantages of SBF

are its transparency and computational efficiency; it requires few parameters, scales effectively to large rasters, and integrates readily with other refinement steps. Comparative studies consistently identify the use of a single global slope threshold as the principal limitation of slope-based filtering. (Bailey et al., 2022) demonstrated that a modified slope-based filter achieved the highest ground-point precision among three tested algorithms but exhibited the lowest overall agreement, due to the inability of a single threshold to accommodate both smooth and rough surfaces. C. Chen, Guo, et al. (2021) reported similar findings for high-density point clouds over heterogeneous landscapes, and Asal (2024) observed the same limitation for slope-based filters applied to aerial-imagery DSMs in rural areas, where above-ground objects and genuine terrain relief could not be separated by a single threshold. In large-scale mapping across Indonesia and Southeast Asia, this pattern is well documented. Kerong et al. (2022) reported strong threshold sensitivity when generating DTMs from aerial photogrammetry over mixed settlement and vegetation cover; Sulung & Soeksmantono (2025) found that adaptive-TIN and cloth-simulation filters outperformed simpler geometric rules on Indonesian LiDAR blocks; and Raj et al. (2024) highlighted the challenges of terrain extraction in densely vegetated riparian corridors.

Recent literature presents two primary responses to this limitation. The first approach is parameter adaptation, where thresholds or window sizes are derived from the data rather than predetermined. For instance, Y. Li et al. (2021) varied grid resolution adaptively using an Octree–KD-tree index; J. Chen et al. (2023) determined local slope thresholds based on within-cell elevation statistics and k-means clustering; Zheng et al. (2024) constructed a two-level adaptive grid using point density and terrain slope to recover seed points on discontinuous terrain; and Niu et al. (2025) divided the process into a surface-fitting stage followed by residual filtering with an adaptive slope criterion. Parallel research on cloth simulation has pursued similar objectives by implementing multi-resolution or self-tuning simulations (Cai et al., 2023). The second approach involves replacing geometric rules with learned classifiers. Point-based networks for forested UAV LiDAR (B. Li et al., 2022), Point CNN-type architectures for agricultural environments (Fareed et al., 2023), and voxel-based deep networks for dense point clouds (Štroner et al., 2025) currently represent the state of the art, supported by large labeled benchmarks such as OpenGF (Qin, Tan, Ma, et al., 2023). Although learned filters achieve the highest reported accuracies, they require labeled training data and computational resources that are often unavailable in operational mapping contexts. Furthermore, Qin, Tan, Ma, et al. (2023) demonstrated that generalization across terrain types and sensor modalities remains unresolved. This limitation is particularly pronounced for photogrammetric point clouds compared to LiDAR data. A third, less explored, approach is to retain the slope rule while making the processing domain adaptive rather than the threshold. This involves first determining the surface type for each pixel and then applying the threshold appropriate to that specific surface. This strategy is particularly appealing for the SBF family because the two primary non-terrain classes in mixed campus, peri-urban, and rural-settlement environments exhibit contrasting geometric characteristics. Vegetation canopies are geometrically rough at meter scales and can be distinguished using local elevation dispersion (Fan & Zhao, 2024). In contrast, building roofs are as smooth as the underlying ground and are identifiable primarily by the abrupt vertical discontinuity at their perimeter, which manifests as a strong image edge (Lu et al., 2018; Hou & Li, 2024). A filter that accounts for this duality can apply a permissive threshold in genuinely steep, vegetated terrain and a strict threshold in flat areas where steep features correspond to building walls.

This study develops the aforementioned concept into a comprehensive, reproducible workflow. The approach is evaluated using an oblique UAV survey of a tropical campus that intentionally incorporates dense secondary vegetation, multi-story buildings, open fields, and 70 meters of relief within a single 121-hectare block. The specific objectives are: (i) to formulate a dual-scheme adaptive SBF in which processing domains are delineated automatically from a roughness raster and an edge-density raster derived solely from the DSM, without ancillary spectral or multi-return data; (ii) to visually characterize the resulting DTM, with particular attention to the void-filling behavior following aggressive non-terrain removal; and (iii) to quantify vertical accuracy against independent check points and to explicitly state the implications and limitations of this accuracy metric. The contribution is not a claim of superiority over learned filters, but rather a demonstration that a raster-domain, two-descriptor zoning step restores much of the adaptivity lacking in conventional SBF, with negligible computational cost and parameters that practitioners can readily inspect and interpret.

2 Study area and data

2.1 Study area

The study area encompasses approximately 121 hectares of the Institut Teknologi Sumatera campus in Jati Agung District, South Lampung Regency, Lampung Province, Indonesia, as shown in Fig. 1. This site was selected because it contains, within a single contiguous block, three distinct land-cover conditions that frequently challenge single-threshold ground filters. The built environment consists of multi-story teaching buildings with flat and low-pitched roofs, hard-standing parking areas, and paved roads. Dense secondary vegetation, including remnant plantation and

regrowth shrub with closed canopy, occupies substantial patches between the built clusters. Open ground, such as sports fields, cleared plots, and the margins of a retention pond, provides unobstructed surfaces for checkpoint establishment. The total relief across the block is approximately 70 meters, indicating that the terrain is not flat. This characteristic is significant, as a filter calibrated to remove all steep features indiscriminately would compromise the integrity of the genuine topography.



Fig. 1 Location of the study area on the ITERA campus with the distribution of the twelve independent check points overlaid on the orthophoto

2.2 UAV acquisition and photogrammetric processing

Aerial imagery was collected using a DJI Mavic 3 Enterprise multirotor platform. An oblique acquisition strategy was implemented, employing camera tilt angles of 45°, 90°, and 135° to enhance the reconstruction of vertical façades and mitigate the systematic occlusion commonly observed at the base of tall objects in near-nadir image blocks. The images were processed in Metashape, utilizing structure-from-motion (SfM) alignment, followed by bundle adjustment and multi-view stereo (MVS) densification at high quality with mild depth filtering. This configuration was selected to preserve fine terrain detail, accepting some reconstruction noise as a trade-off. The resulting products and their associated quality metrics are presented in Table 1.

Table 1 Specifications of the UAV photogrammetric dataset used as input to the filtering workflow

Parameter	Value
Acquisition date	19 February 2025
Platform / camera tilt	DJI Mavic 3 Enterprise; 45°, 90°, 135° (oblique)
Coordinate reference system	WGS 84 / UTM zone 48S
Flying height above take-off	122 m
Orthomosaic ground resolution	4.15 cm pixel^{-1}
Mean reprojection error	0.166 pixel
Coverage of the photogrammetric block	2.45 km²
Study block used for filtering	approx. 121 ha
DSM grid spacing	8.29 cm pixel^{-1}
Point density of the dense cloud	145 points m^{-2}
DSM vertical RMSE at check points	0.144 m
DSM vertical LE90 at check points	0.238 m

The gridded digital surface model (DSM) at 8.29 cm resolution, rather than the unstructured point cloud, serves as the input for the filtering algorithm. Operating within the raster domain is a deliberate methodological choice, as it enables the direct application of neighborhood statistics, edge detection, and morphological reasoning using standard image-processing operators. This approach also constrains memory consumption for datasets of this density. The primary limitation is the potential loss of sub-canopy returns that a point-based filter might capture; however, this limitation is minimal for photogrammetric clouds under closed tropical canopy, since such returns are generally absent.

2.3 Reference check points

Twelve independent checkpoints (ICPs) were surveyed using a CHC S10 GNSS receiver in network RTK mode, with positions distributed throughout the block as shown in Fig. 1. The selection of twelve points adheres to SNI 8202:2019, the Indonesian national standard for base-map accuracy, which requires a minimum of twelve checkpoints for mapped areas smaller than 250 km². All checkpoints were established on open, unobstructed ground to ensure reliable GNSS solutions and to guarantee that the surveyed elevations corresponded directly to the bare-earth surface.

3 Methods

3.1 Overview

The workflow in Fig. 2 comprises five distinct stages. Two descriptors are derived in parallel from the digital surface model (DSM): a surface-roughness raster and an edge-density raster. A rule-based zoning procedure integrates these descriptors into a scheme map, assigning each pixel to either Scheme A (variable terrain) or Scheme B (flat terrain). The slope raster is thresholded using the value specific to each pixel's assigned scheme, and the resulting binary mask is refined through morphological operations. Pixels designated as no-data are subsequently filled using hybrid interpolation, after which a Gaussian filter is applied to smooth transitions between observed and interpolated surfaces. All processing was performed in Python 3 with the NumPy, SciPy, scikit-image, and Rasterio libraries on GDAL (GDAL/OGR contributors 2024), executed in Jupyter Notebook on a workstation featuring an Intel Core i9 (12th generation) CPU, 32 GB RAM, and an NVIDIA GeForce RTX 3070 Ti GPU. A conventional single-threshold SBF implementation in SAGA GIS was used as the baseline for developing the adaptive formulation.

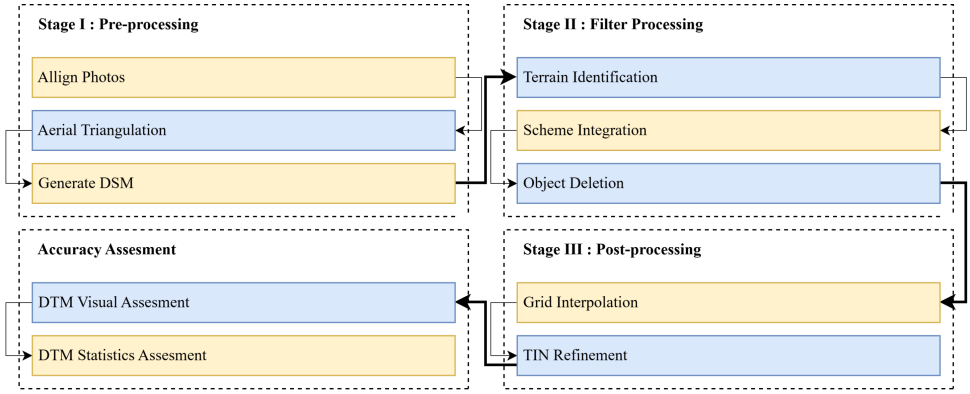


Fig. 2 Workflow of the dual-scheme adaptive slope-based filtering method

3.2 Surface roughness (Scheme A descriptor)

Vegetation canopies differ from both bare ground and roof surfaces in their local elevation dispersion. Following the roughness-descriptor comparison of Fan & Zhao (2024), roughness R at pixel (i, j) is computed as the standard deviation of DSM elevations within a square window W of side k:

$$R_{i,j} = \sqrt{\frac{1}{k^2}\sum_{(p,q)\in W_{i,j}} \left(Z_{p,q} - \bar{Z}_{W_{i,j}}\right)^2} \qquad (1)$$

where $Z_{p,q}$ is the DSM elevation of a pixel inside the window and $\bar{Z}_{W_{i,j}}$ is the window mean. A window of $k = 9$ pixels (81 cells, approximately 0.75 m × 0.75 m at the working resolution) was adopted after testing. (Fan & Zhao, 2024) used $k = 5$ for LiDAR-derived DEMs; on the present 8.29 cm photogrammetric grid, a 5-pixel window responds to reconstruction noise and to genuine micro-relief on bare ground, producing a speckled roughness field that propagates spurious detections into the mask. Enlarging the window to 9 pixels suppresses this response while remaining small enough to resolve the boundary between a canopy patch and adjacent open ground. The choice therefore reflects the grid spacing and noise characteristics of the input rather than a universally preferable value; on a coarser DSM the equivalent metric window would correspond to a smaller k.

3.3 Edge density (Scheme B descriptor)

Roughness alone cannot isolate buildings, because a flat roof and the ground beside it are both smooth. What distinguishes a building is the vertical discontinuity at its perimeter. The edge-density descriptor exploits this. The normalized DSM is first passed through a Canny detector (Canny, 1986), which returns a binary raster E marking

pixels at which the elevation gradient changes abruptly. A mean filter of side $m = 7$ then converts this binary edge map into a continuous density field:

$$D_{i,j} = \frac{1}{m^2} \sum_{(p,q) \in W_{i,j}} E_{p,q} \qquad (2)$$

with $D_{i,j} \in [0,1]$, where 0 indicates a neighborhood free of edges and values approaching 1 indicate a neighborhood saturated with them. The 7-pixel window is deliberately smaller than the roughness window: building outlines are thin, linear features, and a larger averaging kernel dilutes their signal into the surrounding flat ground. Compared with the edge-extraction network of (Lu et al., 2018), which was tuned to recover every sharp boundary in the scene, the present configuration is intentionally conservative — it responds to the strong, closed outlines of building footprints and largely ignores weaker edges such as curb lines and path margins, which is the desired behavior when the objective is to remove structures rather than to map them.

3.4 Rule-based scheme zoning

The two descriptors are combined into a scheme raster *S* by a rule set that is deliberately simple and inspectable:

$$S_{i,j} = \begin{cases} 1 & \text{(Scheme A, variable terrain)} \quad \text{if } R_{i,j} > R_t \\ 2 & \text{(Scheme B, flat terrain)} \quad \text{otherwise} \end{cases} \qquad (3)$$

Every pixel is initialized to Scheme B; pixels whose roughness exceeds the threshold R_t are reassigned to Scheme A. The edge-density raster *D* is then used as a refinement layer within Scheme B, flagging the perimeters of built structures without transferring them to the vegetation domain — a flat roof is a flat surface and belongs geometrically within Scheme B, even though it is not terrain. The zoning raster is thus a control surface, not a classification product: it does not decide what terrain is, only which threshold will make that decision.

3.5 Scheme-dependent slope thresholding

Slope is computed from the DSM in degrees by finite differences over a 3 × 3 neighborhood, and each pixel is compared against the threshold assigned by its scheme:

$$M_{i,j} = \begin{cases} 1 & \text{(non-terrain)} \quad \text{if } S_{i,j} = 1 \text{ and } \theta_{i,j} > \theta_A \\ 1 & \text{(non-terrain)} \quad \text{if } S_{i,j} = 2 \text{ and } \theta_{i,j} > \theta_B \\ 0 & \text{(terrain)} \quad \text{otherwise} \end{cases} \qquad (4)$$

Candidate thresholds of 23°, 25°, 28°, 30°, 31° and 32° were evaluated for Scheme A and 15°, 17°, 18° and 20° for Scheme B, the ranges being bounded below by the steepest slopes observed on unvegetated terrain in the block and above by the point at which canopy edges began to survive filtering. The adopted values were $\theta_A = 25°$ and $\theta_B = 15°$. The asymmetry is the substance of the method: in the vegetated domain the terrain beneath is itself steep, so a permissive threshold is required to avoid stripping genuine relief, whereas in the flat domain any slope beyond a gentle grade is almost certainly a wall or a curb, so a strict threshold is both safe and necessary to capture building perimeters. Three morphological operations then consolidate the raw mask. Binary dilation with a small structuring element thickens detected object outlines, ensuring that the mask fully covers the transition zone at an object boundary rather than clipping its edge. Border handling prevents erroneous fill propagation at the raster margin. Binary hole filling closes interiors enclosed by non-terrain pixels, converting a detected building outline into a solid footprint—without this step, a flat roof, having neither high roughness nor internal steep slopes, would be retained as false terrain at roof height. The final mask *M* partitions the raster into terrain to be preserved and non-terrain to be removed.

3.6 Void filling and surface refinement

Masked pixels are set to no-data, producing a perforated terrain raster. Filling proceeds in two passes for reasons of both quality and memory economy. The first pass applies inverse-distance-weighted interpolation (Shepard, 1968) through *rasterio.fill.fillnodata* with a maximum search distance of 500 pixels (approximately 41 m), which resolves the large majority of voids by drawing on valid terrain pixels around their perimeters. A second pass applies nearest-neighbor interpolation via *scipy.interpolate.griddata* to any cells the first pass could not reach, guaranteeing a gap-free output. The hybrid arrangement is a pragmatic compromise: a single high-quality interpolator applied to voids of this size on a raster of this extent proved prohibitively expensive in memory, whereas IDW alone leaves residual gaps at the centers of the largest vegetated patches. A Gaussian filter is finally applied to smooth the discontinuity between observed and interpolated surfaces.

3.7 Accuracy assessment

Assessment combined a qualitative and a quantitative component, in line with normal practice for filtered terrain products (Sithole & Vosselman, 2004; Qin, Tan, Guan, et al., 2023). The visual assessment examined contours generated from the output DTM for the two failure signatures that filtering and interpolation produce. Contours

running straight across an area that should be gently undulating indicate that interpolation has replaced terrain with a planar fill; sharply serrated contours indicate that the interpolated surface is noisy or that residual non-terrain pixels survive within it. The quantitative assessment compared DTM elevations with the twelve ICP elevations. Vertical RMSE is

$$\mathrm{RMSE}_z = \sqrt{\frac{1}{n}\sum_{i=1}^{n}\left(Z_{\mathrm{DTM},i} - Z_{\mathrm{ref},i}\right)^2} \qquad (5)$$

where n = 12, $Z_{\mathrm{DTM},i}$ is the DTM elevation at check point i, and $Z_{\mathrm{ref},i}$ is the GNSS elevation. This is converted to the 90 % linear error following SNI 8202:2019:

$$\mathrm{LE90} = 1.6449 \times \mathrm{RMSE}_z$$

The same statistics were computed for the input DSM at the same checkpoints, so that the effect of filtering could be isolated from the accuracy already present in the photogrammetric reconstruction. Because Eq. 6 propagates RMSE, which aggregates systematic and random components, it should be read as a summary tolerance rather than as a decomposition of the error; Sect. 4.6 returns to this point.

4 Results and Discussion

4.1 Roughness raster

The roughness raster as shown in Fig. 3 separates the scene into two clearly differentiated populations. Low values, between 0 and approximately 0.25 m of local standard deviation, occupy open ground, roads, sports fields and building roofs — surfaces that are internally homogeneous over the 9-pixel window regardless of whether they are terrain. High values, in the range 1.25–1.75 m, form two spatial patterns: compact patches coinciding with tree canopies, whose upper surface is intrinsically irregular, and narrow linear features tracing building walls, where the window straddles a large elevation step.

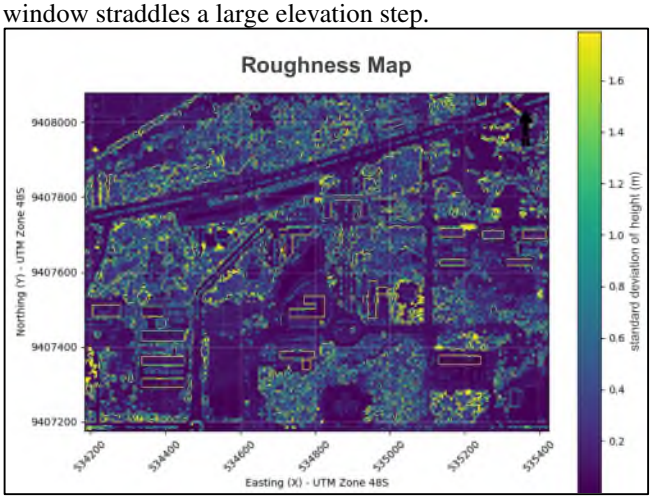


Fig. 3 Surface roughness raster computed as the local standard deviation of DSM elevation in a 9×9 window

Based on Fig. 3, the presence of building walls in the high-roughness class is expected and is the reason a second descriptor is required. Roughness answers the neighborhood's internal irregularity, which is true both of a canopy and of the edge of a roof. It cannot distinguish them, and it is silent about the roof interior. The comparison with (Fan & Zhao, 2024) is instructive here: their 5-pixel window on LiDAR-derived DEMs produced a more sensitive but noisier field, in which minor elevation fluctuations on open ground registered as roughness and subsequently as false non-terrain detections. The 9-pixel window trades some sensitivity to small shrubs for a substantially cleaner separation of the two dominant classes, which is the correct trade when the descriptor's role is zoning rather than classification.

4.2 Edge-density raster

The edge-density raster shown in Fig. 4 is close to zero over the great majority of the block. Values approaching 1 form thin, bright, closed polylines that correspond one-to-one with the outlines of buildings visible in the orthophoto. Flat roof interiors and open ground are indistinguishable in this raster; both are edge-free, which is precisely the intended behavior: the descriptor is designed to locate structure perimeters, not structure areas.

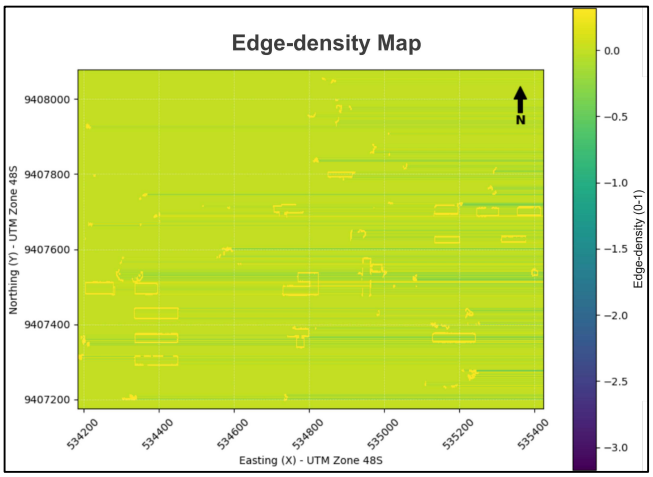


Fig. 4 Edge-density raster obtained by Canny edge detection on the normalized DSM followed by 7×7 mean filtering

The result in Fig.4 differs from that of Lu et al. (2018), whose richer convolutional edge network recovered essentially every sharp boundary in high-resolution imagery, including road margins and field boundaries. The present configuration responds only to the strongest discontinuities. For a mapping objective, this would be a deficiency; for a filtering objective, it is an advantage, because weak edges on the ground surface are not features that should be removed, and a more sensitive detector would push them into the non-terrain mask. The complementarity of the two descriptors is what makes the zoning step work. Ground and roof both have low roughness; ground and roof interior both have low edge density. But a roof is surrounded by a high-edge-density perimeter, and open ground is not; this contextual difference—low roughness enclosed by a high-density ring—that identifies a building without any spectral information.

4.3 Scheme classification raster

The zoning raster in Fig. 5 partitions the block into two logical domains. Scheme B occupies most of the area: open terrain, roads, fields, and building roofs, together with the building perimeters that the edge-density refinement highlights. Scheme A appears as scattered clusters that correlate strongly with the closed-canopy vegetation identified independently in the roughness raster.

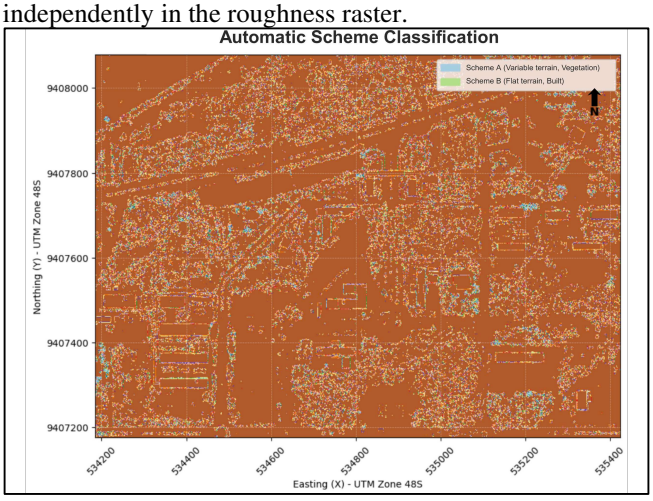


Fig. 5 Automatic scheme classification raster: Scheme A (variable terrain, vegetation) and Scheme B (flat terrain, built and open surfaces)

According to Fig.5, the raster should be read as a control surface rather than as a land-cover map. It does not assert that Scheme A pixels are vegetation and Scheme B pixels are ground; it asserts only that the geometry of Scheme A pixels warrants a permissive slope threshold and that of Scheme B pixels a strict one. This distinction matters when interpreting the errors that follow. A steep, unvegetated slope assigned to Scheme B will be over-filtered, and a low

shrub on flat ground assigned to Scheme B may be missed; both are zoning errors, not thresholding errors, and both would be addressed by improving the descriptors rather than by adjusting θ_A or θ_B.

4.4 Non-terrain mask and the contribution of the dual-scheme formulation

The final mask in Fig. 6 shows buildings resolved as solid blocks rather than hollow outlines, confirming that dilation and hole filling successfully converted perimeter detections into complete footprints. This behavior is consistent with the building-extraction results of (Hou & Li, 2024), obtained there with a Mask R-CNN, and the vegetation component is consistent with the canopy masking of (Khan & Jung, 2024) using an attention-augmented U-Net — although the present method reaches comparable geometric outcomes through explicit geometric rules rather than learned features, and consequently without training data.

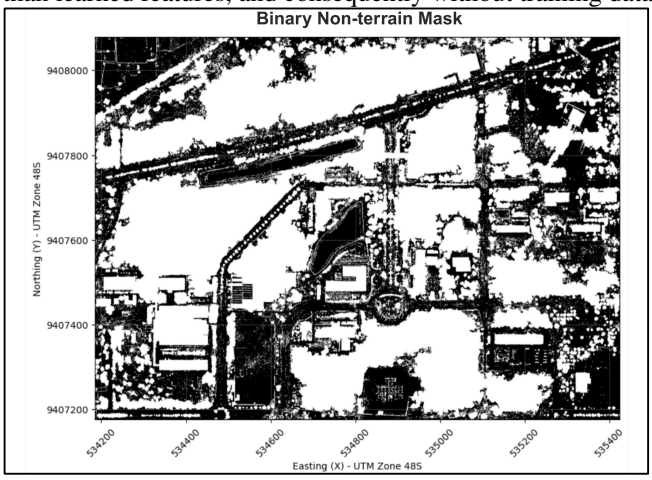


Fig. 6 Binary non-terrain mask. White pixels are classified as non-terrain and removed; black pixels are retained as terrain

Roads, open fields, and parking areas are correctly retained as terrain across the block. Vegetated areas, however, are masked as large contiguous white regions. This is the intended detection outcome and simultaneously the origin of the method's principal weakness: an area removed in its entirety leaves no interior terrain observations to constrain the surface that must replace it. The central result these rasters establish is that the geometric adaptivity conventional SBF lacks can be restored without abandoning the slope rule, by making the *domain* adaptive rather than the threshold. Conventional single-threshold SBF faces an unresolvable trade-off in a scene of this composition: a threshold permissive enough to preserve 70 m of natural relief will leave building walls and canopy edges standing, and a threshold strict enough to remove them will erode the terrain. The dual-scheme formulation dissolves the trade-off by recognizing that the two failure modes occur in spatially separable parts of the scene, and it identifies those parts using descriptors computed from the DSM alone. This positions the method between two established strategies. Statistical parameter adaptation the local-statistics thresholds of (J. Chen et al., 2023), the multi-resolution grids of (Y. Li et al., 2021), the adaptive seed grids of (Zheng et al., 2024), the self-tuning cloth of (Cai et al., 2023), the two-stage residual filtering of (Niu et al., 2025) — derives a parameter from the data but generally applies a single logic uniformly across the scene. Learned filters (B. Li et al., 2022; Fareed et al., 2023; Štroner et al., 2025) achieve the highest reported accuracies but need labeled training data and, in the photogrammetric case, models trained on the appropriate sensor modality; (Qin, Tan, Ma, et al., 2023) documented how sharply their performance can fall when terrain type or acquisition modality shifts away from the training distribution. The present approach requires neither. Its parameters are few and physically interpretable: a window size that corresponds to a metric footprint, a threshold in degrees that a surveyor can relate to the terrain, and every intermediate raster can be inspected to diagnose a failure. For a mapping unit that must produce DTMs routinely and defend them to a client, that transparency has practical value that raw accuracy figures do not capture. The vegetation and building components of the mask are geometrically comparable to results obtained with learned methods on similar scenes (Hou & Li, 2024; Khan & Jung, 2024), which suggests that a substantial part of the discriminative work in these scenes is carried by geometry that explicit rules can encode.

4.5 Digital terrain model and the void-filling bottleneck

The final DTM shown in Fig. 7 is continuous and gap-free. Buildings and canopy patches present in the DSM have been replaced by terrain surfaces, and the broad topographic form of the block — a fall of approximately 70 m across the site is preserved.

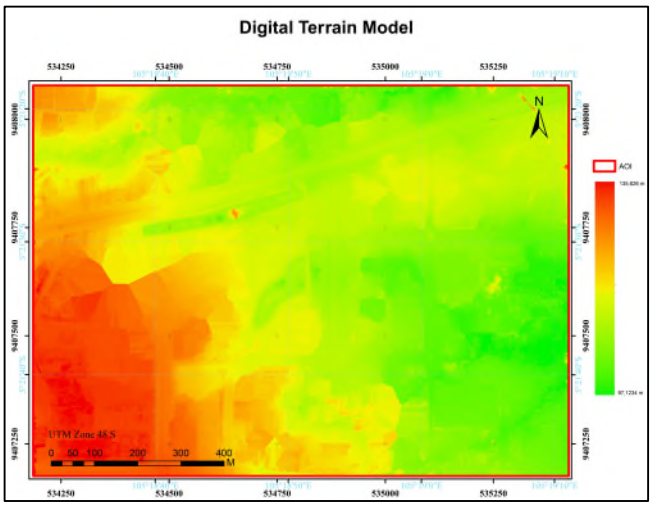


Fig. 7 Digital terrain model produced by the dual-scheme adaptive slope-based filtering workflow

According to Fig. 7, visual inspection nevertheless shows that the interpolated surface inside the largest vegetated patches is coarse. Contours in these areas are broadly plausible in trend but lack the local detail visible on adjacent observed terrain, and in places they run unnaturally straight, the planar-fill signature described in Sect. 3.7. This is a direct and predictable consequence of void extent. Where a masked region spans tens of meters and contains no interior terrain pixels, IDW can only propagate values inward from the perimeter, and the interpolated surface converges toward a smooth ramp between opposing edges. Neither the choice of interpolator nor the Gaussian refinement can recover information that the filtering step removed.

The clearest limitation is not classification but reconstruction. Once large vegetated patches are removed in their entirety, the interior of each void contains no terrain observation whatsoever, and the DTM there is entirely an interpolation product. The hybrid IDW–nearest-neighbor scheme guarantees a complete raster but cannot manufacture information, and the resulting surface is smooth in a way that real terrain is not. The behavior is predictable from the geometry of the fill. An IDW estimate at the center of a void is a distance-weighted average of the perimeter elevations, so it reproduces the mean plane through the perimeter and suppresses any interior convexity or concavity. The magnitude of the resulting error therefore scales with the departure of the true surface from that plane, which grows with void radius and with local terrain curvature. In this block, where relief reaches 70 m and the largest masked patches span several tens of meters, an interior gully or spur crossing a void is simply not represented — an error of decimetre to meter order in the worst cases, although the present validation design cannot measure it directly.

The immediate implication is that the interpolator is the wrong place to look for improvement. A better interpolator natural neighbor, kriging, spline, or a learned inpainting model would produce a smoother or more plausible fill, but the fill would still be unconstrained by observation. Two avenues are more promising. The first is to reduce void extent at source by preserving whatever sub-canopy terrain evidence exists in the photogrammetric cloud rather than masking whole canopy patches wholesale; the point-cloud domain retains low returns at canopy gaps that the rasterized DSM has already discarded through its surface-first representation, a point made concretely for photogrammetric meshes by (Yu et al., 2022). The second is to accept that photogrammetry cannot see beneath a closed tropical canopy and to fuse it with a modality that can. Kang et al. (2026) has been quantified directly: over dense summer vegetation, their best photogrammetric DTM reached an RMSE of 0.179 m against 0.165 m for LiDAR, and they observed that photogrammetric ground points were simply absent beneath low vegetation, whereas multi-return LiDAR retained them. Raj et al. (2024) reported the same asymmetry for densely vegetated riparian corridors in Southeast Asia. There is a design consequence here that generalizes beyond this study. For photogrammetric input, a ground filter should probably be evaluated not only on classification accuracy but on the *spatial distribution of surviving terrain observations*, because a filter that is correct everywhere but leaves no observations inside large object patches produces a DTM whose quality is set by the interpolator rather than by the filter.

4.6 Vertical accuracy and the error budget

Comparison against the twelve ICPs gives a vertical RMSE of 0.148 m for the filtered DTM, corresponding to an LE90 of 0.244 m shown in Table 3. The input DSM, evaluated at the same points, gives 0.144 m and 0.238 m.

Table 3 Vertical accuracy of the input DSM and the filtered DTM at twelve independent check points

Product	$RMSE_z$ (m)	LE90 (m)	Increment relative to DSM (m)
Input DSM (photogrammetric)	0.144	0.238	—
Filtered DTM (this study)	0.148	0.244	+0.004

The 0.004 m increment is smaller than the DSM grid spacing (0.083 m), smaller than the nominal vertical precision of a network-RTK GNSS observation (typically 0.02–0.03 m), and far smaller than the residual scatter that produces an RMSE of 0.148 m in the first place. It is therefore not a resolvable quantity at this sample size, and the defensible statement is that filtering produced no detectable degradation of vertical accuracy on observed terrain, not that it degraded accuracy by 4 mm. The error budget set out below develops both the reasoning behind this reading and the parts of the scene it does not cover.

The vertical accuracy result deserves a more careful reading than a single RMSE value invites, and it is worth setting out the error budget explicitly. The elevation error observed at a check point is the sum of four contributions: (i) the error already present in the photogrammetric reconstruction, propagated from image measurement, camera calibration and bundle adjustment; (ii) a grid-sampling term, since the DTM value is a cell average at 8.29 cm spacing and the GNSS elevation is a point measurement; (iii) a filtering term, which is zero at a pixel correctly retained as terrain and equal to the interpolation residual at a pixel that was masked; and (iv) the reference error of the GNSS observation itself. At the twelve ICPs, all of which lie on open ground that the filter retained, term (iii) is essentially zero by construction. The measured DTM error is therefore dominated by terms (i), (ii) and (iv), the same terms that dominate the DSM error at the same points.

This explains why the DSM and DTM figures are nearly identical, and it explains the sign and size of the small increment. Two operations can perturb a retained terrain pixel: Gaussian smoothing, which slightly attenuates genuine local relief, and mask dilation, which can extend a detected object boundary a short distance onto adjacent ground so that a nearby cell inherits an interpolated rather than an observed value. Both act to raise the residual slightly, which is consistent with the +0.004 m observed. Neither is large enough to resolve against a validation noise floor set by GNSS precision of roughly 0.02–0.03 m, so the honest conclusion is that the filtering and interpolation chain caused no measurable loss of fidelity where terrain was directly observed. That is a meaningful and non-trivial finding; an over-aggressive filter or a poorly conditioned interpolator would have degraded these values by centimeters, and many do, but it is a statement about the absence of collateral damage, not about performance in the difficult parts of the scene. The accuracy that remains unmeasured is precisely the accuracy inside the vegetated voids, where the visual assessment indicates the surface is weakest and where term (iii) is the dominant contribution. Its magnitude cannot be inferred from the ICP statistics, but the published record indicates it is substantially larger: (Kang et al., 2026) reported 0.179 m for a well-filtered photogrammetric DTM over dense vegetation against 0.147 m on bare ground at the same site, an increase of roughly 20 %, with voids smaller than those generated here. A conservative expectation for the present product is therefore that error inside large vegetated voids is at least of that order and, where local curvature is strong, considerably greater.

Three further caveats bear on the statistics themselves. First, twelve points is the regulatory minimum under SNI 8202:2019, not a statistically comfortable sample: an RMSE estimated from twelve residuals carries a wide confidence interval, and differences of a few millimeters between two products evaluated on the same twelve points are well inside it. Second, Eq. 6 propagates RMSE, which combines systematic and random error, so a product with a small bias and a product with equivalent random scatter yield the same LE90; reporting mean error and standard deviation alongside RMSE would separate the two and is recommended for any repetition of this work. Third, the study is a single-site experiment, and the adopted thresholds of 25° and 15° are calibrated to this terrain, this canopy structure, and this building stock. For future work of this kind, we would recommend a stratified validation design in which checkpoints are allocated deliberately across land-cover strata, with the vegetated stratum referenced by terrestrial or mobile laser scanning where GNSS cannot penetrate, complemented by cross-validation of the interpolated surface against terrain pixels withheld from the fill. Only such a design can characterize the error where it actually matters.

4.7 Parameter sensitivity and transferability

Four parameters govern the workflow: the roughness window k, the edge-density window m, and the two slope thresholds θ_A and θ_B. Their behavior is not equally consequential. The two window sizes are tied to the metric resolution of the input. At 8.29 cm grid spacing, $k = 9$ corresponds to a footprint of roughly 0.75 m large enough to average out reconstruction noise, small enough to resolve a canopy edge. A DSM at 0.5 m spacing would require $k =$ 3 or 5 for an equivalent footprint. Reporting these windows in pixels alone, as is common, obscures the fact that the appropriate value is a physical length, not a pixel count. The slope thresholds are the parameters a practitioner would most need to re-derive, and they are also the ones whose sensitivity we have characterized least fully. Candidate values were evaluated qualitatively across 23°–32° and 15°–20°, and the adopted pair was selected on the visual quality of

the resulting mask; a formal sensitivity analysis against a manually classified reference of the kind (Klápště et al., 2020) conducted across filtering algorithms for UAV photogrammetric and LiDAR clouds would place the choice on a firmer footing and would quantify how sharply performance degrades away from the optimum. We regard this as the most important methodological gap in the present study. Transferability is likewise constrained. The zoning logic assumes that vegetation is geometrically rough and that built structures are smooth interiors bounded by strong edges. This holds for the campus, peri-urban and rural-settlement landscapes common in Indonesia and elsewhere in the humid tropics (Kerong et al., 2022; Sulung & Soeksmantono, 2025). It would hold less well over uniform low crops with no roughness signal, over steep bare badlands where terrain roughness rivals canopy roughness, or over informal settlements with irregular, non-planar roofs. Extending the method to such settings would require additional or different descriptors rather than re-tuned thresholds.

4.8 Comparison with alternative filtering families

The results should be compared with what other algorithm families achieve on comparable data. Cloth simulation filtering (W. Zhang et al., 2016) and its recent refinements (Cai et al., 2023) are less parameter-sensitive than classical SBF and generally outperform it on complex terrain; (Bailey et al., 2022) measured $\kappa = 0.86$ for CSF against 0.62 for a modified slope-based filter on high-density terrestrial data. TIN densification remains the operational default in commercial software and continues to be improved for steep and discontinuous terrain (N. Chen et al., 2023; H. Li et al., 2021; Zheng et al., 2024). Learned filters exceed all of these on benchmark data (B. Li et al., 2022; Qin, Tan, Ma, et al., 2023; Štroner et al., 2025). The present method is not offered as a replacement for any of them. Its claim is narrower and, we would argue, more useful: within the slope-based family, spatial domain adaptation recovers a substantial part of the gap to more sophisticated methods at negligible computational and conceptual cost, using only descriptors derivable from the DSM itself. Where a raster DSM is the available product as it frequently is when photogrammetric processing is outsourced, or when only derived products are archived a method that operates entirely in the raster domain has an operational advantage that point-based algorithms do not offer. A controlled comparison against CSF, progressive TIN densification and a learned filter, on the same block and against a manually classified reference, is the obvious and necessary next step, and we did not undertake it here.

5 Conclusions

This study developed a dual-scheme adaptive slope-based filter that assigns each pixel of a UAV photogrammetric DSM to a vegetation-dominated or a flat-terrain processing domain, using a surface-roughness raster and an edge-density raster as complementary descriptors, and then applies the slope threshold appropriate to that domain. Applied to a 121 ha tropical campus block combining dense vegetation, multi-storey buildings and 70 m of relief, the method: (1) separated terrain from buildings and vegetation using geometry alone, resolving buildings as solid footprints after morphological consolidation and delineating canopy patches consistently with the independent roughness signal; (2) produced a gap-free DTM with a vertical RMSE of 0.148 m and an LE90 of 0.244 m at twelve independent GNSS check points; the 0.004 m increment over the input DSM lies below the resolving power of a twelve-point validation, so filtering and hybrid interpolation caused no detectable loss of elevation fidelity on observed terrain; and (3) remained visually deficient inside large vegetated patches, where complete removal of the canopy left no interior terrain observations and the interpolated surface degenerated toward the mean plane through the void perimeter. The limiting factor is therefore reconstruction, not classification. The accuracy figure reported here characterizes open terrain, where the check points necessarily lie, and does not characterize the vegetated interiors where the model is weakest; readers should not extrapolate it to those areas. Priorities for further work are, in order: preserving sub-canopy terrain evidence in the point-cloud domain so that voids are smaller and interpolation is better constrained; a formal sensitivity analysis of the slope thresholds against a manually classified reference; a stratified validation design that measures error within vegetated strata using laser-scanned reference surfaces; and a controlled comparison against cloth simulation, TIN densification and learned filters on the same dataset.

Statements and Declarations

Funding. No funding was received for conducting this study.

Competing interests. The authors have no relevant financial or non-financial interests to disclose.

Ethics approval. Not applicable. This study did not involve human participants or animals.

Consent to participate / Consent to publish. Not applicable.

Data availability. The digital surface model, the derived roughness, edge-density, scheme-classification and non-terrain-mask rasters, the final digital terrain model, and the independent check-point coordinates that support the findings of this study are available from the corresponding author on reasonable request.

Code availability. The Python implementation of the dual-scheme adaptive filtering workflow is available from the corresponding author on reasonable request.

Author contributions. Conceptualization: Muhammad Ulin Nuha, Musa Damar Hadi; Methodology: Muhammad Ulin Nuha, Musa Damar Hadi, Rizqi Aulia; Software and formal analysis: Musa Damar Hadi; Investigation and data curation: Muhammad Ulin Nuha, Musa Damar Hadi; Writing — original draft: Muhammad Ulin Nuha, Musa Damar Hadi, Rizqi Aulia; Writing — review and editing: Muhammad Ulin Nuha, Rizqi Aulia; Supervision: Muhammad Ulin Nuha, Rizqi Aulia. All authors read and approved the final manuscript.

Acknowledgements. The authors thank the Geomatics Engineering Study Program, Institut Teknologi Sumatera, for institutional support, and Almukantar Group for providing access to the oblique photogrammetric acquisition and the check-point survey used in this study.

References

Asal, F. (2024). Evaluating The Effectiveness Of The Dtm Slope-Based Filter In Stripping Off Above Ground Objects From Digital Aerial Imagery Dsm In Rural Landscapes. *Journal of Al-Azhar University Engineering Sector*, *19*(71), 495–513. https://doi.org/10.21608/auej.2024.261004.1584

Bailey, G., Li, Y., McKinney, N., Yoder, D., Wright, W., & Herrero, H. (2022). Comparison of Ground Point Filtering Algorithms for High-Density Point Clouds Collected by Terrestrial LiDAR. *Remote Sensing*, *14*(19), 4776. https://doi.org/10.3390/rs14194776

Cai, S., Yu, S., Hui, Z., & Tang, Z. (2023). ICSF: An Improved Cloth Simulation Filtering Algorithm for Airborne LiDAR Data Based on Morphological Operations. *Forests*, *14*(8), 1520. https://doi.org/10.3390/f14081520

Canny, J. (1986). A Computational Approach to Edge Detection. *IEEE Transactions on Pattern Analysis and Machine Intelligence*, *PAMI-8*(6), 679–698. https://doi.org/10.1109/TPAMI.1986.4767851

Cao, D., Wang, C., Du, M., & Xi, X. (2024). A Multiscale Filtering Method for Airborne LiDAR Data Using Modified 3D Alpha Shape. *Remote Sensing*, *16*(8), 1443. https://doi.org/10.3390/rs16081443

Chen, C., Chang, B., Li, Y., & Shi, B. (2021). Filtering airborne LiDAR point clouds based on a scale-irrelevant and terrain-adaptive approach. *Measurement*, *171*, 108756. https://doi.org/10.1016/j.measurement.2020.108756

Chen, C., Guo, J., Wu, H., Li, Y., & Shi, B. (2021). Performance Comparison of Filtering Algorithms for High-Density Airborne LiDAR Point Clouds over Complex LandScapes. *Remote Sensing*, *13*(14), 2663. https://doi.org/10.3390/rs13142663

Chen, J., Kang, C., Zhang, S., Lan, Y., & Yang, J. (2023). A slope filtering method for point cloud of dense vegetation terrain based on airborne LiDAR. In C. Zuo (Ed.), *International Conference on Remote Sensing, Surveying, and Mapping (RSSM 2023)* (p. 34). SPIE. https://doi.org/10.1117/12.2682654

Chen, N., Wang, N., He, Y., Ding, X., & Kong, J. (2023). An improved progressive triangular irregular network densification filtering algorithm for airborne LiDAR data. *Frontiers in Earth Science*, *10*, 1015153. https://doi.org/10.3389/feart.2022.1015153

Fan, L., & Zhao, Y. (2024). Comparing roughness maps generated by five typical roughness descriptors for LiDAR-derived digital elevation models. *AIMS Geosciences*, *10*(2), 228–241. https://doi.org/10.3934/geosci.2024013

Fareed, N., Flores, J. P., & Das, A. K. (2023). Analysis of UAS-LiDAR Ground Points Classification in Agricultural Fields Using Traditional Algorithms and PointCNN. *Remote Sensing*, *15*(2), 483. https://doi.org/10.3390/rs15020483

Hou, T., & Li, J. (2024). Application of mask R-CNN for building detection in UAV remote sensing images. *Heliyon*, *10*(19), e38141. https://doi.org/10.1016/j.heliyon.2024.e38141

Kang, H., Khoshelham, K., Shin, H., Lee, K., & Lee, W. (2026). Comparative Assessment of Vegetation Removal for DTM Generation and Earthwork Volume Estimation Using RTK-UAV Photogrammetry and LiDAR Mapping. *Drones*, *10*(1), 30. https://doi.org/10.3390/drones10010030

Kerong, R. G. D., Tjahjadi, M. E., & Agustina, F. D. (2022). Kajian Perbandingan Akurasi DTM Pengolahan Data Foto Udara Menggunakan Metode Otomatis Dan Semi-Otomatis Filtering. *Jambura Geoscience Review*, *4*(1), 69–85. https://doi.org/10.34312/jgeosrev.v4i1.12046

Khan, B. A., & Jung, J.-W. (2024). Semantic Segmentation of Aerial Imagery Using U-Net with Self-Attention and Separable Convolutions. *Applied Sciences*, *14*(9), 3712. https://doi.org/10.3390/app14093712

Klápště, P., Fogl, M., Barták, V., Gdulová, K., Urban, R., & Moudrý, V. (2020). Sensitivity analysis of parameters and contrasting performance of ground filtering algorithms with UAV photogrammetry-based and LiDAR point clouds. *International Journal of Digital Earth*, *13*(12), 1672–1694. https://doi.org/10.1080/17538947.2020.1791267

Kraus, K., & Pfeifer, N. (1998). Determination of terrain models in wooded areas with airborne laser scanner data. *ISPRS Journal of Photogrammetry and Remote Sensing*, *53*(4), 193–203. https://doi.org/10.1016/S0924-2716(98)00009-4

Li, B., Lu, H., Wang, H., Qi, J., Yang, G., Pang, Y., Dong, H., & Lian, Y. (2022). Terrain-Net: A Highly-Efficient, Parameter-Free, and Easy-to-Use Deep Neural Network for Ground Filtering of UAV LiDAR Data in Forested Environments. *Remote Sensing*, *14*(22), 5798. https://doi.org/10.3390/rs14225798

Li, H., Ye, C., Guo, Z., Wei, R., Wang, L., & Li, J. (2021). A Fast Progressive TIN Densification Filtering Algorithm for Airborne LiDAR Data Using Adjacent Surface Information. *IEEE Journal of Selected Topics in Applied Earth Observations and Remote Sensing*, *14*, 12492–12503. https://doi.org/10.1109/JSTARS.2021.3131586

Li, Y., Wang, J., Li, B., Sun, W., & Li, Y. (2021). An adaptive filtering algorithm of multilevel resolution point cloud. *Survey Review*, *53*(379), 300–311. https://doi.org/10.1080/00396265.2020.1755163

Li, Z., Zhu, Q., & Gold, C. (2005). *Digital Terrain Modeling: Principles and methodology*. CRC Press.

Lu, T., Ming, D., Lin, X., Hong, Z., Bai, X., & Fang, J. (2018). Detecting Building Edges from High Spatial Resolution Remote Sensing Imagery Using Richer Convolution Features Network. *Remote Sensing*, *10*(9), 1496. https://doi.org/10.3390/rs10091496

Niu, Y., Liu, L., Huang, F., Jiang, Y., & Chen, S. (2025). Research on two-stage point cloud ground filtering algorithm based on slope. In C. Ping (Ed.), *Tenth Symposium on Novel Optoelectronic Detection Technology and Applications* (p. 53). SPIE. https://doi.org/10.1117/12.3055219

Pessacg, F., Gómez-Fernández, F., Nitsche, M., Chamo, N., Torrella, S., Ginzburg, R., & De Cristóforis, P. (2022). Simplifying UAV-Based Photogrammetry in Forestry: How to Generate Accurate Digital Terrain Model and Assess Flight Mission Settings. *Forests*, *13*(2), 173. https://doi.org/10.3390/f13020173

Pingel, T. J., Clarke, K. C., & McBride, W. A. (2013). An improved simple morphological filter for the terrain classification of airborne LiDAR data. *ISPRS Journal of Photogrammetry and Remote Sensing*, *77*, 21–30. https://doi.org/10.1016/j.isprsjprs.2012.12.002

Qin, N., Tan, W., Guan, H., Wang, L., Ma, L., Tao, P., Fatholahi, S., Hu, X., & Li, J. (2023). Towards intelligent ground filtering of large-scale topographic point clouds: A comprehensive survey. *International Journal of Applied Earth Observation and Geoinformation*, *125*, 103566. https://doi.org/10.1016/j.jag.2023.103566

Qin, N., Tan, W., Ma, L., Zhang, D., Guan, H., & Li, J. (2023). Deep learning for filtering the ground from ALS point clouds: A dataset, evaluations and issues. *ISPRS Journal of Photogrammetry and Remote Sensing*, *202*, 246–261. https://doi.org/10.1016/j.isprsjprs.2023.06.005

Raj, P. P. C., Abdul Rahman, M. Z., Ariffin, A., Wan Kadir, W. H., & Suhaili, H. (2024). Integration of Different Density UAV Lidar and Single Beam Echo Sounder (SBES) for River and Riparian Area Digital Terrain Model (DTM) Construction. *Journal of Advanced Geospatial Science & Technology*, *4*(1), 106–129. https://doi.org/10.11113/jagst.v4n1.89

Shepard, D. (1968). A two-dimensional interpolation function for irregularly-spaced data. *Proceedings of the 1968 23rd ACM National Conference On* -, 517–524. https://doi.org/10.1145/800186.810616

Sithole, G., & Vosselman, G. (2004). Experimental comparison of filter algorithms for bare-Earth extraction from airborne laser scanning point clouds. *ISPRS Journal of Photogrammetry and Remote Sensing*, *59*(1–2), 85–101. https://doi.org/10.1016/j.isprsjprs.2004.05.004

Štroner, M., Boušek, M., Kučera, J., Váchová, H., & Urban, R. (2025). Multi-Size Voxel Cube (MSVC) Algorithm—A Novel Method for Terrain Filtering from Dense Point Clouds Using a Deep Neural Network. *Remote Sensing*, *17*(4), 615. https://doi.org/10.3390/rs17040615

Sulung, P. P., & Soeksmantono, B. (2025). Comparative Analysis of DTM Extraction from Airborne LiDAR Point Cloud Data with Adaptive TIN Filter, Cloth Simulation Filter, and Progressive Morphological Filter Methods. *Jurnal Geografi Gea*, *25*(1, April), 1–14. https://doi.org/10.17509/gea.v25i1.71587

Ulfiah, U., Amran Koto, E., & Ningsih, S. (2024). Kebijakan Satu Peta dan Satu Data dalam Program Percepatan Pengadaan Informasi Geospasial Dasar dan Informasi Geospasial Tematik (Kerja Sama Badan Informasi Geospasial Dengan Badan Usaha Milik Negara). *ANTASENA: Governance and Innovation Journal*, *2*(1), 42–53. https://doi.org/10.61332/antasena.v2i1.171

Westoby, M. J., Brasington, J., Glasser, N. F., Hambrey, M. J., & Reynolds, J. M. (2012). 'Structure-from-Motion' photogrammetry: A low-cost, effective tool for geoscience applications. *Geomorphology*, *179*, 300–314. https://doi.org/10.1016/j.geomorph.2012.08.021

Yu, D., He, L., Ye, F., Jiang, L., Zhang, C., Fang, Z., & Liang, Z. (2022). Unsupervised ground filtering of airborne-based 3D meshes using a robust cloth simulation. *International Journal of Applied Earth Observation and Geoinformation*, *111*, 102830. https://doi.org/10.1016/j.jag.2022.102830

Zhang, K., Chen, S.-C., Whitman, D., Shyu, M.-L., Yan, J., & Zhang, C. (2003). A progressive morphological filter for removing nonground measurements from airborne LIDAR data. *IEEE Transactions on Geoscience and Remote Sensing*, *41*(4), 872–882. https://doi.org/10.1109/TGRS.2003.810682

Zhang, W., Qi, J., Wan, P., Wang, H., Xie, D., Wang, X., & Yan, G. (2016). An Easy-to-Use Airborne LiDAR Data Filtering Method Based on Cloth Simulation. *Remote Sensing*, *8*(6), 501. https://doi.org/10.3390/rs8060501

Zheng, J., Xiang, M., Zhang, T., & Zhou, J. (2024). An Improved Adaptive Grid-Based Progressive Triangulated Irregular Network Densification Algorithm for Filtering Airborne LiDAR Data. *Remote Sensing*, *16*(20), 3846. https://doi.org/10.3390/rs16203846